Article

PM$_{2.5}$ Exposure and Health Risk Assessment Using Remote Sensing Data and GIS

Dan Xu [1], Wenpeng Lin [1,2,*], Jun Gao [1,2,*], Yue Jiang [1], Lubing Li [1] and Fei Gao [1]

1   School of Environmental and Geographical Sciences, Shanghai Normal University, Shanghai 200234, China; 1000497916@smail.shnu.edu.cn (D.X.); 1000496184@smail.shnu.edu.cn (Y.J.); 1000459357@smail.shnu.edu.cn (L.L.); 1000496756@smail.shnu.edu.cn (F.G.)
2   Yangtze River Delta Urban Wetland Ecosystem National Field Observation and Research Station, Shanghai 200234, China
*   Correspondence: linwenpeng@shnu.edu.cn (W.L.); gaojun@shnu.edu.cn (J.G.)

Abstract: Assessing personal exposure risk from PM$_{2.5}$ air pollution poses challenges due to the limited availability of high spatial resolution data for PM$_{2.5}$ and population density. This study introduced a seasonal spatial-temporal method of modeling PM$_{2.5}$ distribution characteristics at a 1-km grid level based on remote sensing data and Geographic Information Systems (GIS). The high-accuracy population density data and the relative exposure risk model were used to assess the relationship between exposure to PM$_{2.5}$ air pollution and public health. The results indicated that the spatial-temporal PM$_{2.5}$ concentration could be simulated by MODIS images and GIS method and could provide high spatial resolution data sources for exposure risk assessment. PM$_{2.5}$ air pollution risks were most serious in spring and winter, and high risks of environmental health hazards were mostly concentrated in densely populated areas in Shanghai-Hangzhou Bay, China. Policies to control the total population and pollution discharge need follow the principle of adaptation to local conditions in high-risk areas. Air quality maintenance and ecological maintenance should be carried out in low-risk areas to reduce exposure risk and improve environmental health.

Keywords: air pollution; PM$_{2.5}$ exposure; health risk; geographic information systems; remote sensing

1. Introduction

Air pollution has been considered a global health priority regarding several Sustainable Development Goals (SDGs), such as Goal 3 (Ensure healthy lives and promote well-being for all at all ages) [1,2]. Fine particulate matter (a diameter of less than 2.5 μm, PM$_{2.5}$) pollution is a common type of air pollution in recent years. According to the China Ecological Environmental Bulletin [3–7], 40~75% cities in China exceeded the standard for ambient air quality (PM$_{2.5}$ < 75 μg/m^3), and on 45~80% of days, PM$_{2.5}$ as the primary pollutant exceeded the standard. One study by Son et al. found that short-term exposure to PM$_{2.5}$ was positively associated with increased risk of mortality [8]. Other studies indicated that the long-term chronic effects of PM$_{2.5}$ may cause cardiovascular diseases such as lung cancer, myocardial infarction, and myocardial ischemia [9–11], and it was an important cause of acute triggering of common respiratory system diseases such as asthma, bronchitis, rhinitis, and upper and lower respiratory tract infections [12–14]. Long-term exposure to PM$_{2.5}$ pollution may lead to slow growth, slow neurological development, and brain dysfunction in children [15,16]. In addition, it may lead to depression and pessimism, and even suicidal behavior [17–19]. Due to its critical impact on health, exposure to PM$_{2.5}$ and health risk assessment has been a critical concern for ensuring healthy lives and promoting well-being.

Int. J. Environ. Res. Public Health **2022**, *19*, 6154

2 of 24

There are various data and methods for quantifying ambient air pollution in recent years. Remote sensing (RS) and Geographic Information Systems (GIS) methods have been increasingly used in environment and health research, with corresponding improvements in the use and accessibility of multi-temporal satellite-derived environmental data [20,21]. Some studies estimated $PM_{2.5}$ concentration and spatial-temporal distribution from air quality monitoring stations using spatial interpolation techniques from GIS [22–24], but this approach ignored the uneven distribution of monitoring stations and the rough spatial resolution of the data. The rapid development of RS technology and advanced satellite sensors (with particulate matter detection instruments) addressed this issue. Many satellites (e.g., GOES, Terra, Aqua, METOP, PARASOL) equipped with multifunctional sensors (e.g., MODIS, AVHRR, SeaWiFS, POLDER) greatly promoted the development of Aerosol Optical Depth (AOD, one of the most important parameters of aerosols) inversion by remote sensing imagery interpretation and processing [25–29]. Kaufman introduced the dark target algorithm of AOD inversion based on band relationships [30], and Levy et al. improved the accuracy of AOD inversion of the algorithm [31]. Tanré and Holben developed the structural function method by using atmospheric transmittance to obtain aerosol information [32,33]. Hsu et al. directly adopted surface reflectance data on visibles band to retrieve AOD using the deep blue algorithm [34,35]. Lyapustin et al. proposed a new correction algorithm for AOD inversion, the multi-angle atmospheric correction algorithm, using time series analysis and image processing technology for atmospheric correction and AOD inversion [36,37].

Many researchers found a specific relationship between AOD and $PM_{2.5}$ that could be estimated by some methods from AOD to $PM_{2.5}$ [38–40]. The model correction method used different models to correct various influencing factors and simulate the proportion relationship between AOD and $PM_{2.5}$, such as the atmospheric chemical transport model (GEOS-Chem) [41–43] and the atmospheric boundary layer model (RAMS) [44]. However, this method ignored the physical mechanism between AOD and $PM_{2.5}$. Both aerosol type and vertical distribution lead to differences in scattering extinction. The mechanism correction method solved this problem and obtained the stable aerosol extinction coefficient by vertical correction and scattering extinction correction for $PM_{2.5}$ estimation [45–48]. However, this method was highly dependent on setting physical mechanism parameters, and these parameters are different in different areas. In order to monitor and estimate $PM_{2.5}$ in real time, it is necessary to update these physical mechanism parameters in time. In addition, the statistical model method established linear or nonlinear statistical models between the AOD and $PM_{2.5}$ based on various meteorological or environmental elements (wind speed, direction, position, humidity, height, etc.), such as multiple linear regression model (GLM) [49,50], generalized summation model (GAM) [51,52], and geographically weighted regression model (GWR) [53–57]. Some researchers combined several statistical models to construct multilevel statistical models to estimate $PM_{2.5}$ concentration. In recent years, the machine learning (ML) method has been widely used to associate AOD with $PM_{2.5}$, incorporating big geographic spatial-temporal data as examples and with self-supervision and training functions [58,59]. Although this method had high accuracy in estimating results and could deal with the complex relationship between AOD and $PM_{2.5}$, it required multistep processing of training samples in advance and relevant operations on physical and chemical mechanisms, which increased the difficulty of use to a certain extent [60]. Many methods have associated AOD with $PM_{2.5}$, each with its characteristics.

To explore the relationship between $PM_{2.5}$ air pollution and health exposure risk, one study by Zou et al. found a spatial pattern of population exposure to air pollution by constructing a relative exposure risk assessment model [61]. Tong et al. showed that population density data and the relative exposure risk assessment model could more reasonably represent the relationship between $PM_{2.5}$ pollution and environmental health [62]. Lu et al. developed a personal mobility model to quantify long-term

air pollution exposure for individuals [63]. Park developed an air dispersion model based on a large sample of travel-activity diary data to assess personal exposure to $PM_{2.5}$ [64]. These studies confirmed the applicability to and efficiency of remote sensing data and GIS for exposure to $PM_{2.5}$ air pollution and environmental health. However, risk assessment results from these studies were not sufficiently accurate owing to the limited availability of high spatial resolution data for $PM_{2.5}$ and population density.

Toward this end, this study presents a framework that incorporates high spatial resolution remote-sensing images and geographic spatial-temporal data to retrieve AOD and estimate $PM_{2.5}$ based on the GIS platform. The Enhanced Dark Target Algorithm (EDTA) is introduced to retrieve daily AOD from MODIS images, improving the spatial resolution at 1 km grid level. Spatial-temporal seasonal models are used to estimate $PM_{2.5}$ concentration using geospatial-temporal data and GIS spatial analysis methods. Then, we assess the exposure risk to $PM_{2.5}$ pollution using high-accuracy population density data and the relative exposure risk models. Finally, we discuss the usage and deficiency of assessment results and offer our expectations for future application. We look forward to provide scientific reference for improving urban atmospheric pollution and living environment.

2. Materials and Methods

2.1. Study Area

SHB is located in eastern China and the north Pacific coastal area (28°51′~31°53′ N, 118°21′~123°25′ E) and is an important part of the integrated development of the Yangtze River Delta, China. From north to south, it contains seven cities, including Shanghai, Jiaxing, Huzhou, Hangzhou, Shaoxing, Ningbo and Zhoushan. Its total land area is about 52,300 km^2, and its population is about 54.41 million (2018 Statistical Yearbook of China). Belonging to the northern subtropical region, SHB is characterized by a mild and humid climate with abundant rainfall. The terrain is higher in the southwest and lower in the northeast; plains, hills and mountains cover the most part (Figure 1). In 2018, SHB had five of the top 100 cities (in comprehensive strength) in China: Shanghai (no. 2), Hangzhou (no. 5), Ningbo (no. 20), Shaoxing (no. 34), Jiaxing (NO. 39), reflecting the highly developed policy, economy, society, culture, and ecology in SHB.
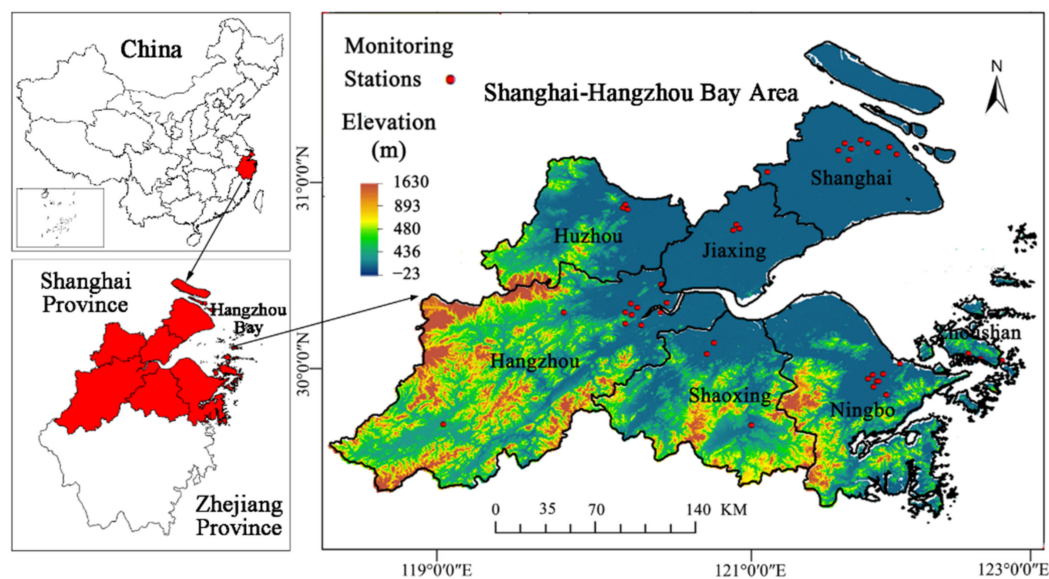

Figure 1. The location and elevation map of the study area, SHB.

2.2. Data Source

2.2.1. Vector and Elevation Data

The data on the region boundaries and elevation were from the Resource and Environmental Sciences and Data Center, China (ESDC, http://www.resdc.cn/Default.aspx, accessed on 18 May 2019).

2.2.2. Remote Sensing Data

Terra MODIS L1B data (Level 1, with Global Certification Level) were applicable and reliable for China [65,66] at a spatial resolution of 1 km ×1 km. Excluding a period of no data from 19 to 27 February, there were 1 to 3 image data every day, for a total of 827 images of original data from SHB from 1 January to 31 December 2016. Data were downloaded from NASA LAADS Web to retrieve AOD (LAADS, https://ladsweb.nascom.nasa.gov/, accessed on 4 December 2019).

2.2.3. Ground-Based AOD Observation Data

The observation error for ground-based AOD from AERONET is 0.01~0.02, which can be used directly for the correction of estimated AOD [67]. The Version 3 and Level 1.5 data (data after cloud processing) in 2016 were downloaded from the Aerosol Robotic Network (AERONET, http://aeronet.gsfc.nasa.gov/, accessed on 18 May 2019) for verifying the accuracy of retrieved AOD. We finally chose Level-1.5 AOD data from two stations (SONET_Shanghai and SONET_Zhoushan) according to the actual situation in SHB (Table 1).

Table 1. Data from AERONET AOD stations in SHB in 2016.

City	Site	Longitude (°E)	Latitude (°N)	Data
Shanghai	SONET_Shanghai	121.481	31.284	Level 1.0 [a], Level 1.5 [b]
	Shanghai_Minhang	121.397	31.130	null
	Shanghai_Met	121.549	31.221	null
Hangzhou	LA-TM	119.440	30.324	null
	Hangzhou-ZFU	119.727	30.257	null
	Hangzhou_City	120.157	30.290	null
	Qiandaohu	119.053	29.556	null
Ningbo	Ningbo	121.547	29.860	null
Zhoushan	SONET_Zhoushan	122.188	29.994	Level 1.0 [a], Level 1.5 [b]

[a] Level 1.0 for original data. [b] Level 1.5 for cloud filtering and quality control data.

2.2.4. Ground-Level $PM_{2.5}$ Observation Data

Based on China national standards and specifications for ambient air quality assessment, daily observation data on $PM_{2.5}$ concentrations (unit: $\mu g/m^3$) at air quality monitoring stations were derived from the official website of the China Environmental Monitoring Center for exploring the optimal relationship between retrieved AOD and $PM_{2.5}$ observation data (CEMC, http://106.37.208.233:20035/, accessed on 23 December 2019). There were 41 monitoring stations in SHB, and specific information is in Table 2.

2.2.5. Population Density Data

The population density data came from the open population data set platform Worldpop (https://www.worldpop.org/, accessed on 23 December 2019), with a spatial resolution of 1 km × 1 km. Based on remote sensing images and geospatial-temporal big data, this data set used the random forest algorithm to simulate the spatial-temporal distribution of the population density, comprehensively considering land cover and land use, residential areas, roads, buildings, public facilities, night lights, vegetation, geographic and geomorphic conditions, and so on [68].

Table 2. Geographical coordinates of PM$_{2.5}$ monitoring stations in SHB.

City	Monitoring Station	Longitude (°E)	Latitude (°N)
Shanghai	Putuo	121.3984	31.2637
	NO.15 Factory	121.3614	31.2228
	Hongkou	121.4919	31.2825
	Shanghai Normal University	121.4232	31.1675
	Sipiao	121.5360	31.2659
	Dianshan Lake	120.9382	31.0927
	Jingan	121.4363	31.2305
	Chuansha	121.7042	31.1994
	Pudong New Area	121.6634	31.2428
	Zhangjiang	121.5918	31.2108
Jiaxing	Qinghe Primary School	120.7543	30.7819
	Jiaxing College	120.7372	30.7517
	Disabled Persons' Federation	120.7739	30.7601
Hangzhou	Binjiang	120.1924	30.1876
	Xixi	120.1000	30.2645
	Qiandao Lake	119.0214	29.6020
	Xiasha	120.3442	30.3221
	Wolong Bridge	120.1385	30.2493
	Zhejiang Agricultural University	119.7355	30.2621
	Zhaohui NO.5 Community	120.1688	30.2940
	Hemu Primary School	120.1312	30.3161
	Linping	120.3133	30.4272
	Chengxiang	120.3052	30.2615
	Yunqi	120.1010	30.1989
Shaoxing	Paojiang	120.6238	30.0842
	East Management Committee of Development Zone	120.8460	29.5986
	Shuxia Wang	120.5828	30.0159
Ningbo	Environmental Protection Building	121.5865	29.8582
	Wanli College	121.5695	29.8230
	Longsai Hospital	121.7223	29.9596
	Sanjiang Middle School	121.5647	29.8940
	Qiangtang Waterwork	121.6440	29.7770
	Taigu Primary School	121.5985	29.8596
	Environmental Monitoring Center	121.5351	29.8709
	Wanli International School	121.6234	29.9019
Zhoushan	Dinghai TanFeng	122.1320	30.0240
	Putuo Donggang	122.3285	29.9791
	Lincheng New Area	122.2020	29.9885
Huzhou	Renhuangshan New Area	120.0976	30.9000
	West Waterwork	120.0844	30.8811
	Wuxing	120.1158	30.8710

2.3. Methods

2.3.1. Enhanced Dark Target Algorithm (EDTA)

The dark target algorithm (DTA) is an operational algorithm with high inversion accuracy and maturity. Kaufman found a good linear relationship between surface reflectivity in the near-infrared band (2.1 μm) and the visible red band (0.66 μm) and visible blue band (0.47 μm) [69]. The near-infrared band is affected very little by aerosols, and its apparent reflectivity can be approximated as surface reflectivity [26]. The surface reflectivity of the visible red and blue bands can be estimated with a linear calculation equation:

$$\rho_r = \frac{1}{2} * \rho_n \tag{1}$$

$$\rho_b = \frac{1}{4} * \rho_n \tag{2}$$

where ρ_r is the surface reflectivity of the visible red band (0.66 μm); ρ_b is the surface reflectivity of the visible blue band (0.47 μm); and ρ_n is the surface reflectivity of near-infrared band (2.1 μm).

Apparent reflectivity is the result of surface reflectivity and atmospheric reflectivity, as shown in Equation (3). The apparent reflectivity information of the visible red and blue bands can be obtained from satellite remote sensing data, and the surface reflectivity of the visible red and blue bands can be obtained after removing the linear estimation, which gives the atmospheric reflectivity [70]:

$$\rho^*(\mu, \varphi, \mu_0, \varphi_0) = \rho_a(\mu, \varphi, \mu_0, \varphi_0) + \frac{T(\mu_0)T(\mu)\rho}{1 - \rho s} \tag{3}$$

where ρ^* is apparent reflectivity; μ is the cosine of the satellite zenith angle, μ_0 is s the cosine of the solar zenith angle, φ is the satellite azimuth angle, φ_0 is the solar azimuth angle; ρ_a is atmospheric reflectivity; $T(\mu_0)$ is the total transmittivity from the sun to the earth's atmosphere; $T(\mu)$ is the total transmittivity from the earth's surface to the satellite's atmosphere; ρ is surface reflectivity; and s is the spherical surface albedo of the atmosphere.

Based on the basic dark target algorithm (DTA), we introduced the enhanced dark target algorithm (EDTA) to retrieve the AOD according to the actual situation in SHB. The basic inversion process included radiometric correction, geometric correction, resampling, composition and clipping, cloud detection and elimination, Lookup Table (LUT) setting, and accuracy verification of the inversion results (Figure 2). We improved the inversion algorithm, especially in building LUT.

Geometry correction. MODIS L1B 1 km data (MOD02_1KM) contains emissivity and reflectivity files and angle data (sensor zenith and sensor azimuth of the satellite, solar zenith and solar azimuth of the sun), which are obviously different types. We employed ENVI software to resample the row and column numbers of angle data set from 271 × 406 to 1354 × 2030 (e.g., emissivity and reflectivity files) before correction. The HDF file was used to generate ground control points (GCPs). The correction model was Triangulation, and the resampling method was Bilinear.

Band operation and cloud detection. The Layer Stacking tool was adopted for synthesizing geometry files and angle data after correction. The stacked order of emissivity and reflectivity files (as well as angle data) affected the results. The reflectivity file must be placed in up and the emissivity file in down. In fact, angle data had been expanded 100 times in HDF files, so it should have been multiplied by 0.01 during band operation. In order to remove the influence of cloud reflection, absorption and scattering noise, the Cloud Detection tool was installed.

LUT Setting and AOD retrieval. The accuracy of LUT determines the accuracy of AOD retrieval to a certain extent. A 6S Radiation Transmission model was used to distinguish various surface types and observation bands. Different parameters of atmospheric aerosol and observation parameters were preset for radiation transmission calculation to obtain inversion results. After geometric correction, band operation, band clipping, cloud detection, and invalid value elimination, the results for emissivity, reflectance, and angle data set were combined with the LUT to perform aerosol inversion calculation, and we obtained AOD inversion values. According to geographical features and the actual situation in SHB, we improved the related model and enhanced the LUT setting in the geometric parameters (Table 3) to produce the enhanced dark target algorithm (EDTA).
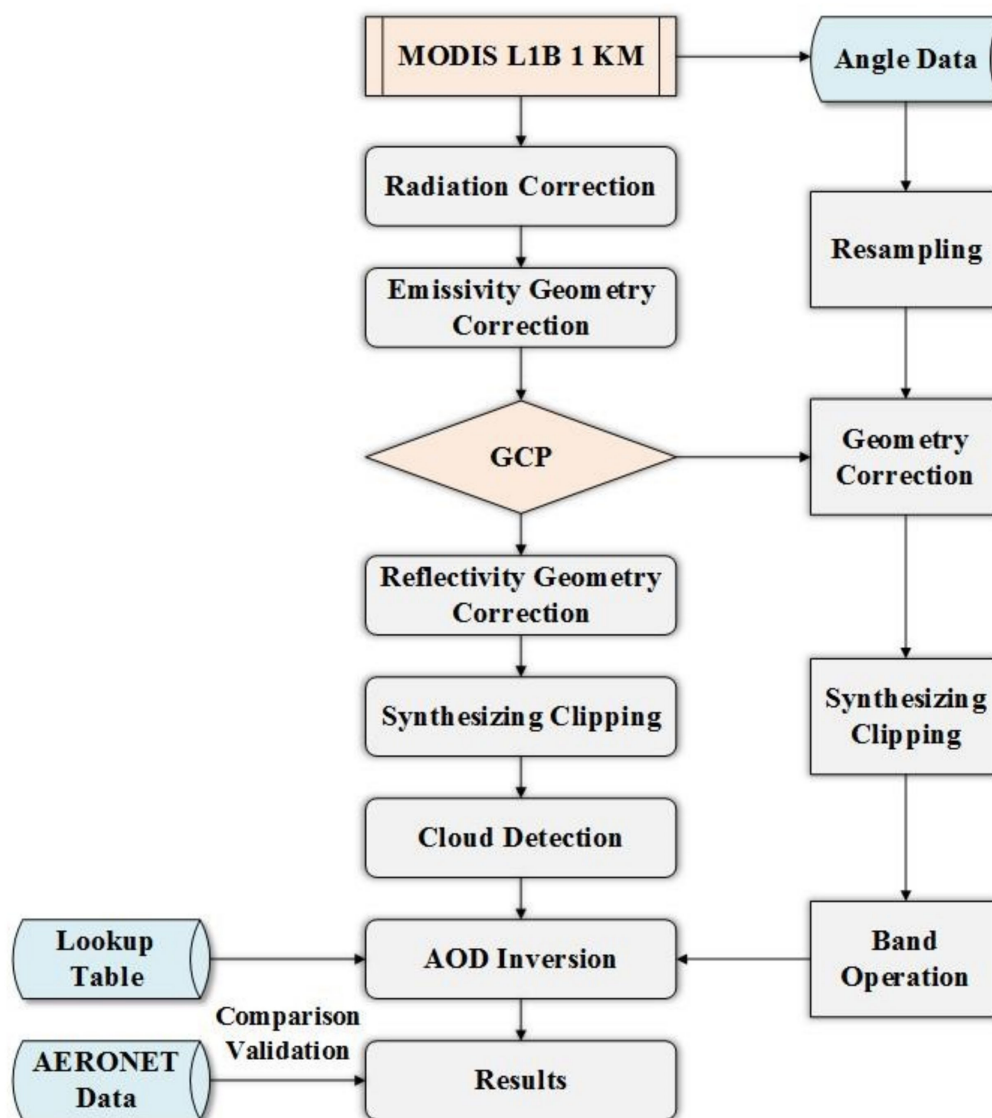
Int. J. Environ. Res. Public Health **2022**, *19*, 6154

7 of 24

Figure 2. The flow chart of AOD inversion.

Table 3. Geometric parameters of LUT based on a 6 S transmission model.

Major Parameters	Settings
Satellite zenith angle	0°, 12°, 24°, 36°, 48°, 60°
Solar zenith angle	0°, 12°, 24°, 36°, 48°, 60°
Relative azimuth angle	0~180°, 24° (interval)
AOD at 550 nm wavelength	0, 0.25, 0.50, 1.00, 1.50, 1.95
Central wavelength	470 nm, 660 nm, 2100 nm
Elevation	0
Surface type	Vegetation

Validation. The ground-based AOD from AERONET data was used to verify the accuracy of the retrieved AOD. We set the value of AOD at 550 nm wavelength (0, 0.25, 0.50, 1.00, 1.50, 1.95) in LUT, but the AERONET data were available in 340 nm, 380 nm, 440 nm, 500 nm, 675 nm, 870 nm, 936 nm, 1020 nm, and 1640 nm wavelength channels (no AOD observation value in 550 nm). Only AOD values of the same observation band

could be compared, so the AOD values of AERONET between different observation band channels needed to be converted. We used the Angstrom formula to convert [71]:

$$\tau_\lambda = \beta * \lambda^{-\alpha} \tag{4}$$

where λ is the wavelength; τ_λ is AOD of the wavelength λ; β is the atmospheric turbidity index; and α is the wavelength index.

2.3.2. AOD-PM$_{2.5}$ Spatial-Temporal Regression Models

When observing the relationships between AOD samples and PM$_{2.5}$ samples, we found that PM$_{2.5}$ tended to increase gradually with increasing AOD. Therefore, AOD samples were taken as the independent variable and PM$_{2.5}$ samples as the dependent variable. In order to infer the relationship between AOD (independent variable) and PM$_{2.5}$ (dependent variable), we mainly used 6 linear and nonlinear regression models, including linear, logarithmic, exponential, power, quadratic polynomial, and cubic polynomial function regression models (Table 4). By combining terrain, landscape, and other geospatial information, we applied and tested each model pixel by pixel based on seasonal characteristics and the actual situation in SHB.

Table 4. Regression models for AOD-PM$_{2.5}$ relationship prediction.

Regression Model	Equation
Linear	$y = a_0 + a_1 x$
Logarithmic	$y = a_0 + a_1 \ln(x)$
Exponential	$y = a_0 \times e^{a_1 x}$
Power	$y = a_0(x^{a_1})$
Quadratic Polynomial	$y = a_0 + a_1 x + a_2 x^2$
Cubic Polynomial	$y = a_0 + a_1 x + a_2 x^2 + a_3 x^3$

x for independent variable. y for dependent variable. a_0, a_1, a_2, a_3 for relevant parameters.

The first part of the AOD samples (estimated from the MODIS images) and the PM$_{2.5}$ samples (observed from the monitoring stations) was used for model modeling, and the second part was used for model testing. The optimal model was determined based on model fit (determinant coefficient, R^2) and error results (root mean square error, RMSE) (Equations (5) and (6)) to build a spatial-temporal estimation model of AOD-PM$_{2.5}$ suitable for SHB and to simulate the spatial-temporal pattern of PM$_{2.5}$ concentration based on the grid:

$$R^2 = \frac{\sum_{i=1}^n (\hat{y}_i - \overline{y})^2}{\sum_{i=1}^n (y_i - \overline{y})^2} \tag{5}$$

$$RMSE = \sqrt{\frac{\sum_{i=1}^n |\hat{y}_i - y_i|^2}{n}} \tag{6}$$

where R^2 is the determine coefficient; $RMSE$ is the root mean square error; n is the sample number; $\hat{y}_i$ is the value of independent variable i; y_i is the value of dependent variable i; and $\overline{y}$ is the mean value of the dependent variable.

2.3.3. Pearson's and Spearman's Rank Correlation Coefficients

Pearson's correlation coefficient (R) was applied to the correlation analysis between observation AOD (ground-based from AERONET) and inversion AOD (estimated from MODIS images), seeing by Equation (7):

$$R = \frac{\sum_{i=1}^n (z_i - \overline{z})(u_i - \overline{u})}{\sqrt{\sum_{i=1}^n (z_i - \overline{z})^2 \sum_{i=1}^n (u_i - \overline{u})^2}} \tag{7}$$

where R is the Pearson correlation coefficient; n is the sample number; z_i is the observation AOD value of i; $\bar{z}$ is the average value of observation AOD; u_i is the inversion AOD value of i; and $\bar{u}$ is the average value of inversion AOD.

Spearman's rank correlation coefficient (ρ) was used to indicate the correlation between estimated AOD and observed $PM_{2.5}$ as in Equation (8):

$$\rho = 1 - \frac{6 \sum_{i=1}^{n}(G_i - H_i)^2}{n(n^2 - 1)} \tag{8}$$

where ρ is the Spearman's rank correlation coefficient, G_i is the rank of estimated AOD; H_i is the rank of observed $PM_{2.5}$ value; is the rank difference of estimated AOD and observed $PM_{2.5}$ value.

2.3.4. Relative Exposure Risk Model

Based on the estimated $PM_{2.5}$ concentration and population density data at 1-km grid level, this study used the relative exposure risk model to assess the resident exposure level to $PM_{2.5}$ air pollution [61,72], as in Equation (9):

$$Q_i = \frac{P_i \times M_i}{\sum_{i=1}^{n} P_i \times \frac{M_i}{n}} \tag{9}$$

where i is the grid number; Q_i is the relative population exposure risk of i; P_i is the population density of i (unit: person/km^2); M_i is the $PM_{2.5}$ concentration of i (unit: $\mu g/m^3$); and n is the total number of grids.

For the convenience of analysis, values of the exposure risk results were divided into six levels referring to previous studies [73,74]: extremely safe ($Q_i = 0$), safe ($0 < Q_i \ll 1$), relatively safe ($1 < Q_i \ll 2$); relatively dangerous ($2 < Q_i \ll 3$), dangerous ($3 < Q_i \ll 5$), and extremely dangerous ($Q_i > 5$).

2.3.5. Spatial Autocorrelation Analysis

Moran's *I* is used to represent the spatial autocorrelation, including the global Moran's *I* and the local Moran's *I*. The global Moran's *I* is for the spatial autocorrelation of variables in the study area as a whole. When the value of *I* approaches 1, the correlation of variables in the spatial distribution is more significant; when the value of *I* approaches 0, the correlation is weaker. The local Moran's *I* refers to the correlation degree between the local area and the surrounding area, and its results can be shown in the LISA agglomeration figure. Its I_i value is calculated by Equations (10) and (11):

$$I_i = \frac{(x_i - \bar{x})}{S_i^2} \sum_{i,j=1}^{n} w_{i,j}(x_j - \bar{x}) \tag{10}$$

$$S_i^2 = \frac{\sum_{i,j=1}^{n}(x_i - \bar{x})^2}{n - 1} \tag{11}$$

where n is the number of grids, $i \neq j$, x_i, and x_j are values of variables of i and j, $\bar{x}$ is the average value, and $w_{i,j}$ is the weight matrix for the proximity between i and j. On the significance test, the significance level is $\alpha = 0.05$.

The Results of I_i are divided into five types for the spatial agglomeration characteristics: HH (high-high) is the high-value agglomeration phenomenon, LL (low-low) is the low-value agglomeration phenomenon, LH (low-high) and HL (high-low) are high values alternate with low values, and NS (not significant) is no obvious agglomeration features.

Int. J. Environ. Res. Public Health **2022**, *19*, 6154

10 of 24

3. Results

3.1. AOD Inversion Results

The value range of AOD inversion results was from 0 to 1.95, which was a dimensionless value. The larger the AOD was, the greater the aerosol optical thickness was, indicating the lower atmospheric transmittance. The 0 value indicated the existence of no aerosol particles, which was the best atmospheric condition and indicated that solar radiation was not reduced when it passed through the atmosphere.

Because the remote sensing images were large and susceptible to cloud influence, the AOD inversion process and results would have been affected by large areas of cloud in those time periods. We screened MODIS images from all of the year of 2016 one by one, and we excluded images that were seriously blurred by clouds. Finally, we obtained monthly AOD results for SHB (from average daily AOD) for February, March, April, May, June, July, August, September, November, and December (10 months in total) and seasonal AOD results (from average monthly AOD) for spring (March, April, May), summer (June, July, August), autumn (September, November), and winter (February, December) in SHB.

3.1.1. Monthly AOD Results

In the monthly AOD results in Figure 3, higher AOD values were concentrated in Shanghai, Jiaxing, northwest of Hangzhou, Shaoxing, and northern Ningbo, and lower AODs were concentrated in southwest and south of SHB, namely, southwest of Hangzhou, south of Shaoxing and Ningbo, and Zhoushan. Because some MODIS images in a certain time were affected by cloud interference, a small portions of them were eliminated and then showed null values. However, this did not affect the inversion results for other regions, so they continued to participate in the calculation. In 2016, the AOD began increasing steadily beginning in February through May and gradually decreased in June and July, reached the lowest in August; then they gradually increased from September to November and reached the peak in December. Therefore, AOD showed a time variation tendency of "high-low-high" in SHB.

3.1.2. Seasonal AOD Results

In the seasonal AOD results in Figure 4, inversion AOD still presented the distribution characteristics of higher at the coast and lower in the south in spatial scale. In terms of time scale, the overall AOD was lowest in summer and highest in winter, with little difference between spring and autumn, and seasonal AOD still presented a high-low-high tendency in SHB. For higher-value coastal regions, the distribution of low and middle values was interphase in summer, the distribution of middle and high values was interphase in winter, and the distribution of middle values was uniform in spring and autumn, indicating that AODs in the coastal regions were greatly different in summer and winter. Moreover, Zhoushan had the lowest AOD throughout all four seasons, indicating the least $PM_{2.5}$ pollution and the best air quality in 2016.

3.1.3. Verification Result

Using Level 1.5 AERONET AOD data (from ground-based AOD observation stations) of "SONET_Shanghai" and "SONET_Zhoushan", we verified the accuracy of the inversion AODs. In 2016, there were 29 days of Level 1.5 data available for SHB. AOD inversion values on those days were extracted through software, and then invalid AOD values (disturbed by clouds) were removed to obtain valid values. Finally, values of inversion AOD and observation AOD could be used for verification, a total of 21 groups of data (Table 5).
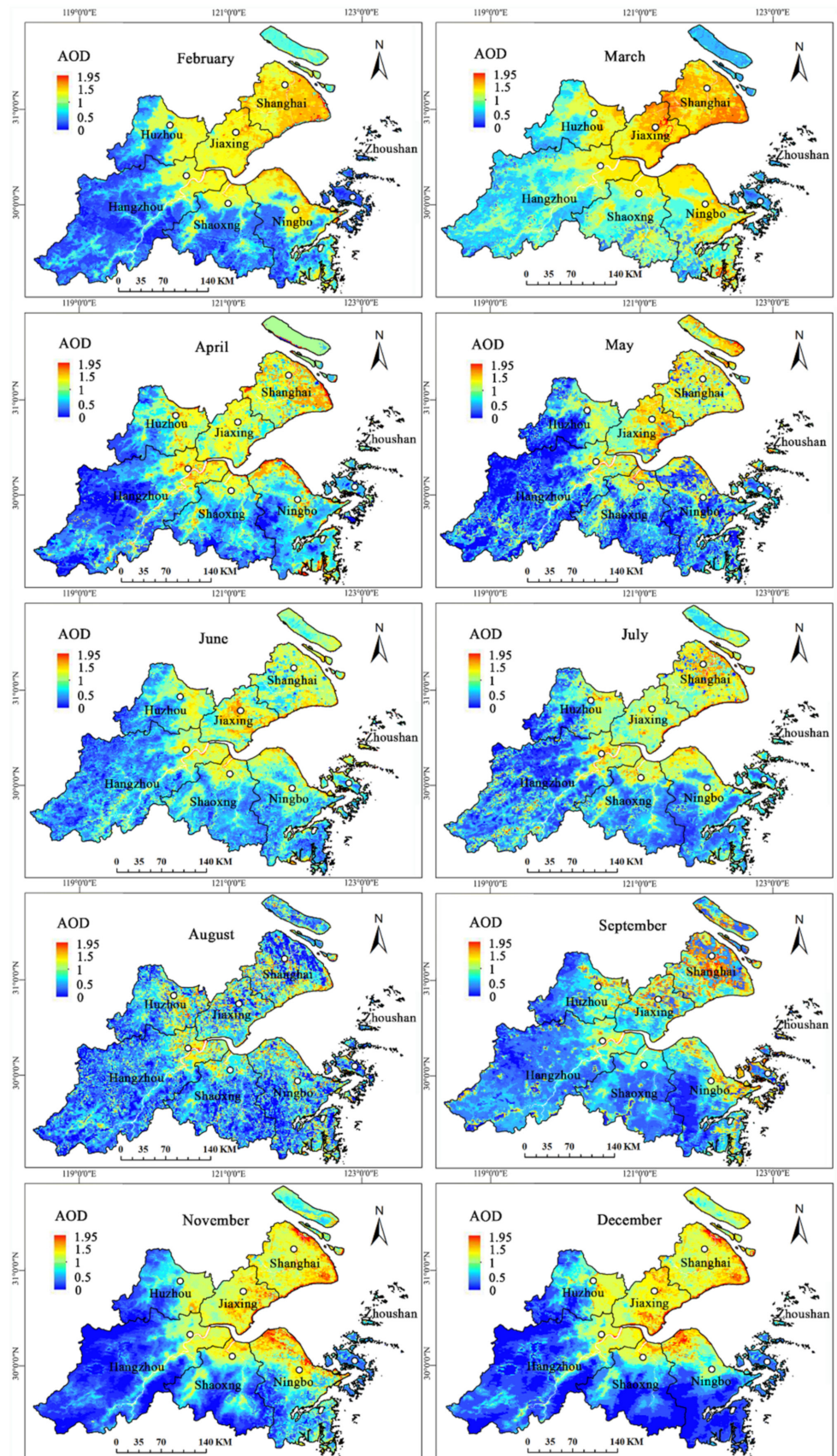
Int. J. Environ. Res. Public Health **2022**, *19*, 6154

11 of 24

Figure 3. Monthly inversion AODs in SHB.

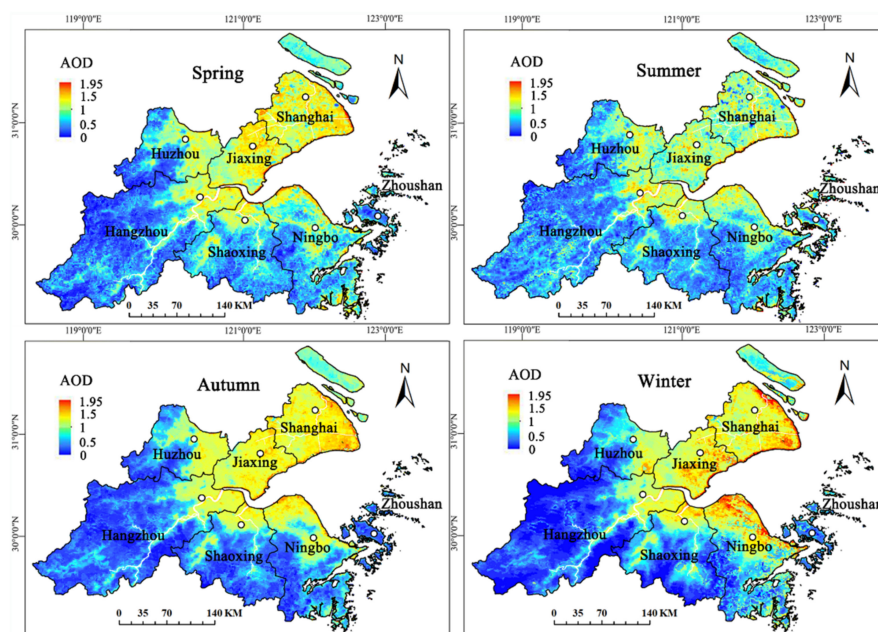*Int. J. Environ. Res. Public Health* **2022**, *19*, 6154

12 of 24

Figure 4. Seasonal inversion AODs in SHB.

Table 5. Pearson correlation analysis of inversion AOD and observation AOD.

Site	Days	Date	AOD Value	
			Inversion	Observation
SONET_Shanghai	10	1 May 2016	0.610	0.785
		3 May 2016	0.792	0.890
		4 May 2016	0.500	0.449
		12 May 2016	0.375	0.304
		15 May 2016	0.400	0.551
		16 May 2016	0.917	0.346
		17 May 2016	0.400	0.222
		24 May 2016	1.170	1.194
		25 May 2016	1.246	0.951
		6 June 2016	0.720	1.153
SONET_Zhoushan	11	30 April 2016	0.808	0.464
		1 May 2016	0.730	0.474
		3 May 2016	0.320	0.314
		4 May 2016	0.700	0.775
		11 May 2016	1.170	0.815
		12 May 2016	0.563	0.534
		16 May 2016	0.200	0.218
		17 May 2016	0.150	0.154
		18 May 2016	0.200	0.199
		24 May 2016	1.000	1.022
		6 June 2016	0.350	0.360
M [a]			0.634	0.580
SD [b]			0.334	0.328
R [c]			0.781	0.781
Significant (bilateral)			0	0

[a] M for mean value. [b] SD for standard deviation. [c] R for Pearson correlation coefficient.

The verification results in Table 5 show that inversion AOD and observation AOD in terms of time trend were approximately the same. From the Pearson's correlation analysis, M and SD for the inversion AOD were higher than those for the observation AODs, and R was 0.781 at the 0.01 significance level, showing that the observation AODs were strongly related to the inversion AODs. The AOD result was at a spatial resolution of 1 km × 1 km.

Therefore, we verified that the inversion AODs obtained by MODIS data and EDTA were relatively accurate, and the inversion results could be used for the estimation of $PM_{2.5}$ concentrations at higher accuracy and resolution.

3.2. Seasonal Spatial-Temporal Models

3.2.1. Correlation Analysis of Inversion AOD and Observation $PM_{2.5}$

Observation $PM_{2.5}$ (from ground-level monitoring stations) was used to explore the relationship with inversion AOD because of its uneven distribution in space. In the observation $PM_{2.5}$ data (Figure 5A), the daily average $PM_{2.5}$ concentration was 42.94 µg/m^3 in 2016, with the highest being 137 µg/m^3 in January and the lowest being in 12.86 µg/m^3 in September. $PM_{2.5}$ concentration decreased gradually from winter to summer and increased gradually from summer to winter. Among all cities (Figure 5B), Huzhou ranked first in 2016, with a monthly average $PM_{2.5}$ concentration of 61.30 µg/m^3, followed by Hangzhou at 45.99 µg/m^3, Shanghai at 44.36 µg/m^3, Shaoxing at 43.82 µg/m^3, Jiaxing at 43.24 µg/m^3, and Ningbo at 37.50 µg/m^3. Concentrations were highest in winter (January and December) and lowest in summer (August). According to the $PM_{2.5}$ concentration air quality standards in China, Zhoushan had the lowest $PM_{2.5}$ concentration of 24.39 µg/m^3 and the most air quality standard days (361 days, $PM_{2.5} < 75$ µg/m^3)(Figure 6), indicating it was the least polluted city in SHB. Shanghai and Hangzhou had two days of severe pollution ($150 < PM_{2.5} \leq 250$ µg/m^3), with maximum $PM_{2.5}$ concentrations of 156 and 165 µg/m^3, respectively. The number of days exceeding the standard from most to least occurred in Huzhou (62 days), Hangzhou (51 days), Shanghai (46 days), Shaoxing (42 days), Jiaxing (39 days), Ningbo (28 days), and Zhoushan (5 days) in 2016 (Figure 6).
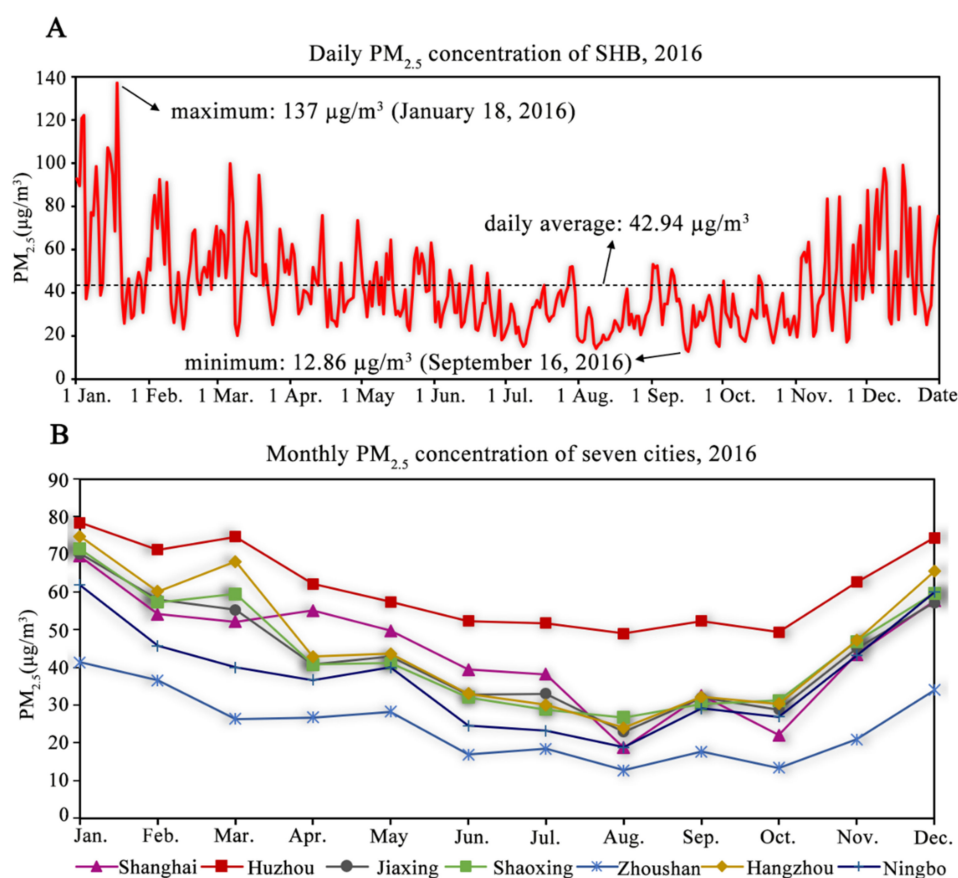
Figure 5. Observations of $PM_{2.5}$ in SHB. (**A**). Daily average $PM_{2.5}$ concentration. (**B**). Monthly average $PM_{2.5}$ concentration of each city.
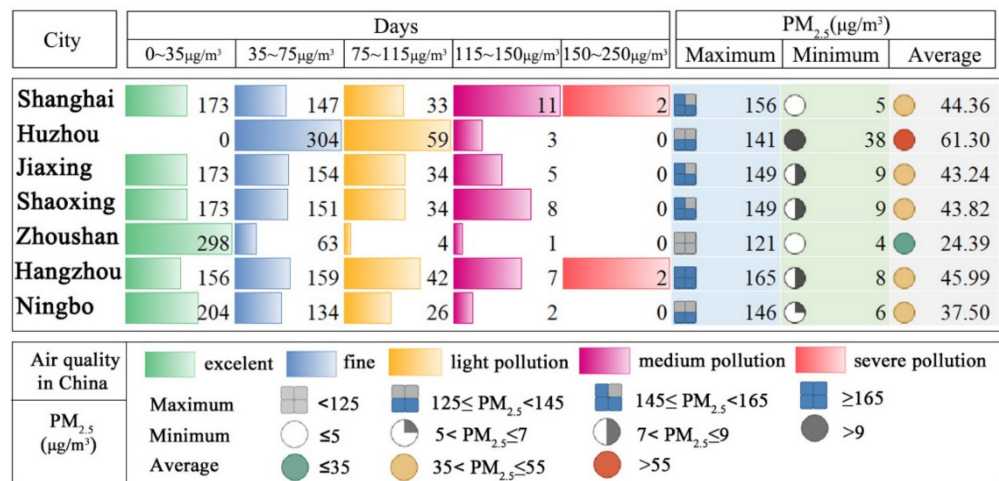
Int. J. Environ. Res. Public Health **2022**, *19*, 6154

14 of 24

Figure 6. Air quality ratings and observed PM$_{2.5}$ concentrations in seven cities.

Values for inversion AOD and observation PM$_{2.5}$ were processed by the min-max normalization method using a total of 410 groups (Table 6). The monthly correlation analysis results showed inversion AOD had the best correlation with observation PM$_{2.5}$ in May, with ρ of 0.631 (at 0.01 confidence level), followed by in August, with ρ of 0.607. Since there was a big difference between inversion AOD and observation PM$_{2.5}$ values every month in 2016, the correlations between them were calculated by season. In the seasonal correlation analysis in Table 6, we found that the best correlation was in summer, with ρ of 0.684 (at 0.01 confidence level), followed by spring, with ρ of 0.538. Overall, PM$_{2.5}$ concentration increased gradually with the increase in AOD. The correlation in each season was better than that in each month. Therefore, seasonal modeling was more effective for PM$_{2.5}$ estimation in SHB.

Table 6. Correlation analysis of inversion AOD and observation PM$_{2.5}$ (at 0.01 confidence level).

Month	Sample	ρ [a]	N [b]	Season	Sample	ρ [a]	N [b]
March	AOD PM$_{2.5}$	0.021	41				
April	AOD PM$_{2.5}$	0.406	41	Spring	AOD PM$_{2.5}$	0.538	123
May	AOD PM$_{2.5}$	0.631	41				
June	AOD PM$_{2.5}$	0.443	41				
July	AOD PM$_{2.5}$	0.432	41	Summer	AOD PM$_{2.5}$	0.684	123
August	AOD PM$_{2.5}$	0.607	41				
September	AOD PM$_{2.5}$	0.395	41	Autumn	AOD PM$_{2.5}$	0.474	82
November	AOD PM$_{2.5}$	0.138	41				
December	AOD PM$_{2.5}$	0.314	41	Winter	AOD PM$_{2.5}$	0.341	82
February	AOD PM$_{2.5}$	0.121	41				

[a] ρ for Spearman's rank correlation coefficient. [b] N for sample size.

3.2.2. Seasonal Model Building and Verification

Based on the correlation analysis of inversion AOD and observation PM$_{2.5}$, we obtained 123 groups of data in spring, 123 groups in summer, 82 groups in autumn, and 82 groups in winter. A part of each season's data was used for model building, and another part was used for model verification. AOD was the independent variable and PM$_{2.5}$ the dependent variable. R^2 represented the model fit degree, and F is for the significance of the model. The larger these values, the more significant and suitable the model is.

In spring, the first 82 groups were used for model building, and the last 35 groups were used for model verification (6 groups of abnormal values eliminated). The seasonal model building results (Figure 7A) show that the power model was the best in spring, with R^2 = 0.511 and F = 77.209. In summer, the first 84 groups were used for model building, and the last 35 groups were used for model verification (4 groups of abnormal values eliminated), and the exponential model was the best in summer, with R^2 = 0.551 and F = 127.519 (Figure 7B). In autumn, the first 41 groups were used for model building, and the last 41 groups were used for model verification, and the power model was the best, with R^2 = 0.524 and F = 34.180 (Figure 7C). In winter, the first 41 groups were used for model building, and the last 41 groups were used for model verification, and the power model was the best, with R^2 = 0.504 and F = 39.556 (Figure 7D).

The seasonal model verification results in Table 7 show that the power model had better fit and the fewest errors in spring, with R^2 = 0.513 and RMSE = 6.204; the exponential model showed the best fit and the smallest error in summer, with R^2 = 0.640 and RMSE = 3.979; the fit of the power model was the best and the error was smaller in autumn, with R^2 = 0.520 and RMSE = 7.893; and the power model had better fit and minimum error in winter, with R^2 = 0.540 and RMSE = 7.392. Overall, the power model was the best in spring, autumn, and winter and the exponential model was the most suitable for summer, showing that both played significant roles in estimating PM$_{2.5}$ concentration, especially the power model. Based on these optimal seasonal models, we combined observation PM$_{2.5}$ concentrations and the geographic big data according to the actual situation and features in SHB to produce seasonal spatial-temporal models for PM$_{2.5}$ estimation.

3.3. PM$_{2.5}$ Estimation Results

Based on these seasonal spatial-temporal models, we obtained seasonal PM$_{2.5}$ estimation results for SHB (Figure 8). Spatially, the PM$_{2.5}$ concentrations in each season showed the same distribution characteristic of higher in the coastal areas and lower in the mountainous areas. Zhoushan was the city with the lowest PM$_{2.5}$ concentration in all seasons, which was always lower than 40 μg/m^3. Shanghai and Jiaxing were both above 40 μg/m^3 in all seasons, making them the two most polluted cities. From the perspective of time, the average PM$_{2.5}$ concentrations over the four seasons was winter > spring > autumn > summer, and the PM$_{2.5}$ concentration showed a high-low-high tendency in a year.

From the annual average PM$_{2.5}$ results in Figure 8E, we see that the PM$_{2.5}$ concentration range was 0~68.16 μg/m^3, and its spatial resolution was 1 km × 1 km. Concentrations were high (50~70 μg/m^3) in Shanghai, Jiaxing, northwest of Hangzhou, Shaoxing, and the northern part of Ningbo; medium (30~50 μg/m^3) in the vicinity of high concentration; and low (0~30 μg/m^3) mainly in the southwest of Hangzhou and Zhoushan. Overall, the spatial distribution of PM$_{2.5}$ concentrations was higher in the northeast and lower in the southwest, indicating that the area along the Hangzhou Bay was seriously affected by fine particles, and the air quality in the mountainous area with higher altitude was better. This correlated with the elevation characteristics of SHB (Figure 1). The coastal areas are of low altitude, with dense populations, convenient transportation, and developed industry and commerce, which is not conducive to haze diffusion. However, the mountainous areas are of high altitude, with high vegetation coverage and abundant rain, so there is less PM$_{2.5}$ pollution and good air quality.
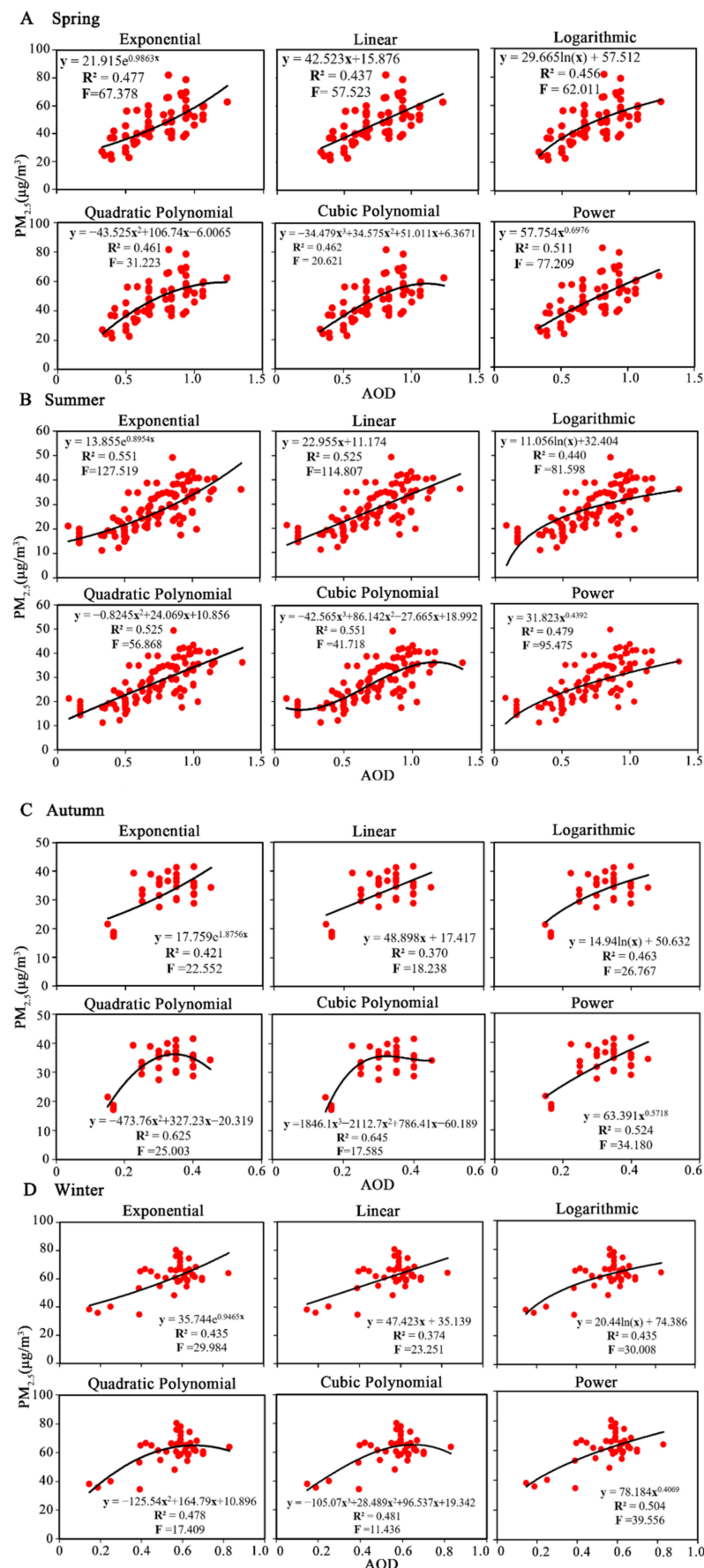
Int. J. Environ. Res. Public Health **2022**, *19*, 6154

16 of 24

Figure 7. Seasonal model-building results. (**A–D**) for spring, summer, autumn, winter, respectively.

Int. J. Environ. Res. Public Health **2022**, *19*, 6154

17 of 24

Table 7. Seasonal model building and verification results.

| Season	Model	Equation	Model Building		Model Verification	
			R^2	F	R^2	RMSE
Spring	A [a]	$y = 42.523x + 15.876$	0.437	57.523	0.514	6.587
	B [b]	$y = 29.665\ln(x) + 57.512$	0.456	62.011	0.503	6.719
	C [c]	$y = 21.915e^{0.9863x}$	0.477	67.378	0.504	6.246
	D [d]	$y = -43.525x^2 + 106.74x - 6.0065$	0.461	31.223	0.506	6.829
	E [e]	$y = -34.479x^3 + 34.575x^2 + 51.011x + 6.3671$	0.462	20.621	0.515	6.900
	F [f]	$y = 57.754x^{0.6976}$	0.511	77.209	0.513	6.204
Summer	A [a]	$y = 22.955x + 11.174$	0.525	114.807	0.590	4.432
	B [b]	$y = 11.056\ln(x) + 32.404$	0.440	81.598	0.418	5.254
	C [c]	$y = 13.855e^{0.8954x}$	0.551	127.519	0.640	3.979
	D [d]	$y = -0.8245x^2 + 24.069x + 10.856$	0.525	56.868	0.588	4.440
	E [e]	$y = -42.565x^3 + 86.142x^2 - 27.665x + 18.992$	0.551	41.718	0.606	4.113
	F [f]	$y = 31.823x^{0.4392}$	0.479	95.457	0.518	4.313
Autumn	A [a]	$y = 48.898x + 17.417$	0.370	18.238	0.488	8.857
	B [b]	$y = 14.94\ln(x) + 50.632$	0.463	26.767	0.515	7.534
	C [c]	$y = 17.759e^{1.8756x}$	0.421	22.552	0.478	8.980
	D [d]	$y = -473.76x^2 + 327.23x - 20.319$	0.625	25.003	0.455	9.010
	E [e]	$y = 1846.1x^3 - 2112.7x^2 + 786.41x - 60.189$	0.645	17.585	0.497	9.087
	F [f]	$y = 63.391x^{0.5718}$	0.524	34.180	0.520	7.893
Winter	A [a]	$y = 47.423x + 35.139$	0.373	23.251	0.508	7.957
	B [b]	$y = 20.44\ln(x) + 74.386$	0.435	30.008	0.547	7.621
	C [c]	$y = 35.744e^{0.9465x}$	0.435	29.984	0.471	7.706
	D [d]	$y = -125.54x^2 + 164.79x + 10.896$	0.478	17.409	0.550	7.450
	E [e]	$y = -105.07x^3 + 28.489x^2 + 96.537x + 19.342$	0.481	11.436	0.553	7.429
	F [f]	$y = 78.184x^{0.4069}$	0.504	39.556	0.540	7.392

x: independent variable. Y: dependent variable. [a] A: The linear regression model. [b] B: The logarithmic regression model. [c] C: The exponential regression model. [d] D: The quadratic polynomial regression model. [e] E: The cubic polynomial regression model. [f] F: The power regression model.

In this work, the spatial distribution result of observation PM$_{2.5}$ concentration was obtained by the Kriging interpolation of GIS, and its optimal spatial scale could only reach 12 km × 12 km (because of the small number of monitoring stations) (Figure 8F). Compared with estimates of PM$_{2.5}$ concentrations from remote sensing data (1 km × 1 km), although PM$_{2.5}$ concentrations are high in similar areas (Shanghai, the junctional zone of Jiaxing, Huzhou, and Hangzhou), the estimated PM$_{2.5}$ concentrations are more continuous and even more accurate in some areas, such as east and west of Huzhou and south and north of Shaoxing. Eastern Huzhou has a larger population and a more developed economy, so the impacts of PM$_{2.5}$ population on eastern areas should be greater than that on western areas. The same is true in the northern and southern areas of Shaoxing. Therefore, PM$_{2.5}$ concentration estimates from remote sensing images are closer to the real situation in SHB, reflecting the necessity of remote sensing to estimate PM$_{2.5}$ for assessing fine pollution levels at a regional scale.

3.4. Exposure Risk Assessment

Based on population density data from Worldpop (1-km grid level) and the relative exposure risk model, the exposure risk to PM$_{2.5}$ pollution was evaluated using GIS. Figure 9A shows that each level of average annual exposure risk was unevenly distributed around the cities, indicating that PM$_{2.5}$ air pollution degree differs greatly around SHB. The range of exposure risk values was from 0 to 133, with a large difference between the lowest value and the highest value. In addition, about 2/3 of the land area was a safe zone, and the rest was in a danger zone (all low-elevation urban areas). By city, the average annual exposure risk was Shanghai (3.57) > Jiaxing (1.24) > Ningbo (0.77) > Shaoxing (0.51) > Hangzhou

(0.50) > Zhoushan (0.46) > Huzhou (0.44). Except for Shanghai, other cities were in the safe range, with residents of Huzhou city the least exposed to $PM_{2.5}$ pollution. Moreover, the danger level of exposure risk in each city was concentrated in the coastal areas around SHB, and the higher elevations (in the south) were all safe, with the lowest $PM_{2.5}$ pollution degree. The highest danger level was mainly concentrated in the main urban areas, with Shanghai and Hangzhou as the most serious.
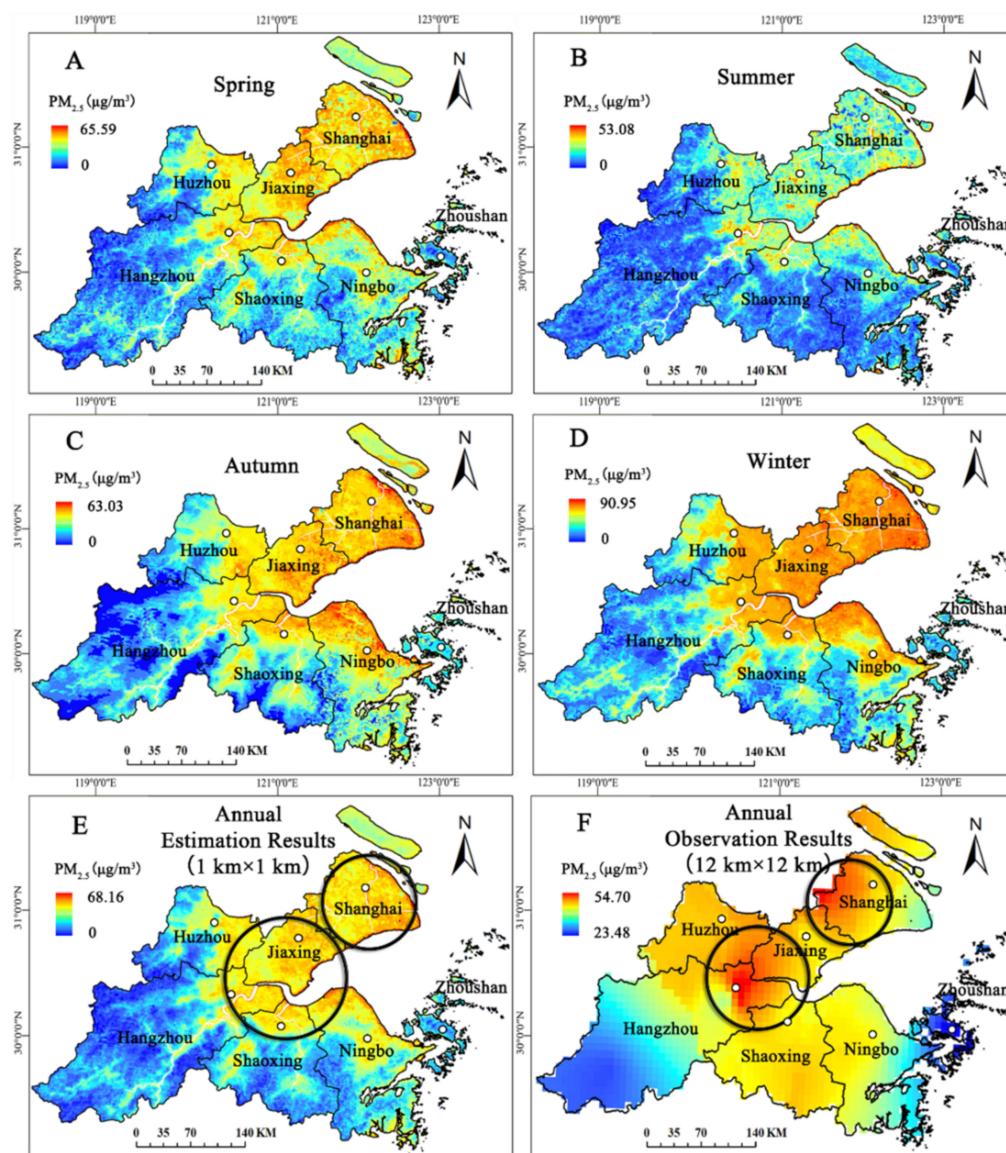
Figure 8. 2016 $PM_{2.5}$ concentration maps for SHB. (**A–D**) Seasonal estimates of $PM_{2.5}$ concentration. (**E**) Annual average estimates of $PM_{2.5}$ concentration (1 km × 1 km). (**F**) Observation $PM_{2.5}$ concentration interpolation results (12 km × 12 km).

On the global Moran's *I* for SHB, the values were 0.6436 in spring, 0.6174 in summer, 0.6365 in autumn, and 0.6351 in winter. Values of *p* for all four seasons were all above 0.01, indicating strong positive spatial correlations and high significance of $PM_{2.5}$ exposure risk in SHB. The results of the LISA spatial aggregation (Figure 9B) indicated that the annual average $PM_{2.5}$ exposure risk in SHB had a strong spatial autocorrelation and an obvious spatial aggregation. The high-value agglomeration (HH) was distributed in Shanghai, northeastern Hangzhou, central Jiaxing, and central Ningbo. The low-value agglomeration (LL) was mainly distributed in the areas with higher elevations, Shanghai and Zhoushan City in the Chongming District. Overall, the coastal areas

Int. J. Environ. Res. Public Health **2022**, *19*, 6154

19 of 24

were dominated by high-value clustering, and mountainous areas were dominated by low-value clustering.
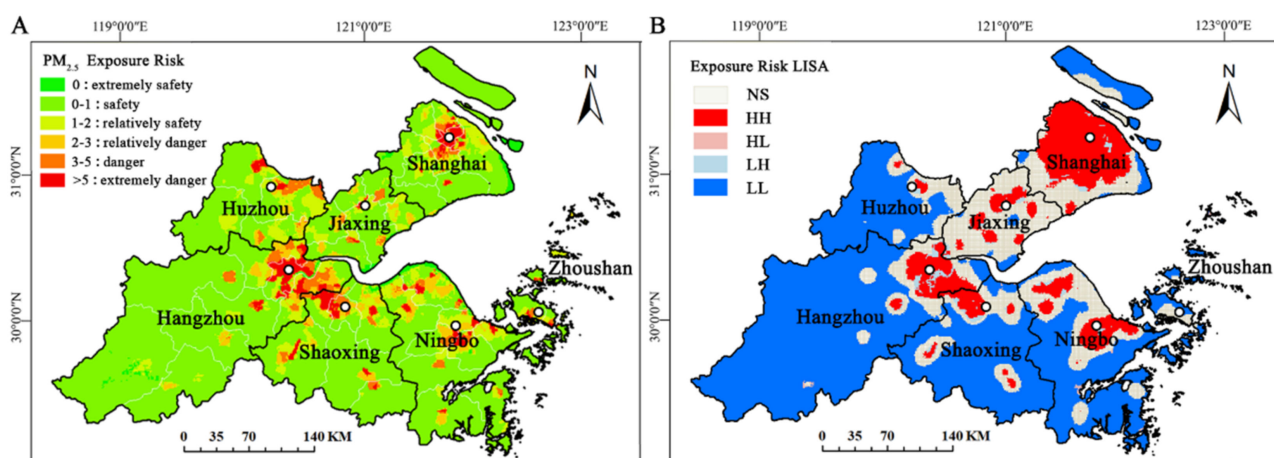

Figure 9. Maps of PM$_{2.5}$ exposure risk (**A**) and LISA agglomeration (**B**) in SHB, China.

4. Discussion

Due to the high cost of construction and maintenance of air quality monitoring stations, the number of stations is small in China. Monitoring stations are unevenly distributed, mostly concentrated in relatively developed areas. The observation PM$_{2.5}$ concentrations could only reflect the local PM$_{2.5}$ situations but could not truly reflect the actual characteristics of spatial distribution. In addition, there are few available, suitable, and high spatial resolution PM$_{2.5}$ products, so we use daily MODIS images and introduce the EDTA method to retrieve high-resolution AODs in space and time to create high-precision and high-resolution PM$_{2.5}$ concentrations at a 1-km grid level based on a seasonal spatial-temporal estimation model. In this work, we addressed problems of the spatial resolution and the spatial-temporal continuity of PM$_{2.5}$ concentration data.

Previous studies that adopt spatial distribution analysis of PM$_{2.5}$ using monitoring station data and GIS interpolation methods only account for local area situations or analyze variations in PM$_{2.5}$ characteristics and time trends using annual average data. Studies using monitoring stations to obtain PM$_{2.5}$ did not take suitable spatial resolution into account; studies using interpolation methods to derive PM$_{2.5}$ did not focus on seasonal differences in PM$_{2.5}$ pollution. Both are not precise enough in time and space.

By introducing the EDTA method and seasonal spatial-temporal models, we estimate the seasonal PM$_{2.5}$ concentration in a high spatial resolution of 1 km × 1 km. The verification accuracy (R^2) of estimation PM$_{2.5}$ concentration reached 0.513 in spring, 0.640 in summer, 0.520 in autumn, and 0.540 in winter, and the estimation error (RMSE) was in the range of 3.979~7.893 μg/m^3. We showed the feasibility and reliability of retrieving AOD and estimating PM$_{2.5}$ from MODIS remote sensing images. According to the characteristics of different seasons, we also constructed a corresponding estimation model that has seasonal applicability. Today, 1 km-grid level of PM$_{2.5}$ concentration is a higher-resolution data source, which could allow for assessing fine PM$_{2.5}$ pollution at small and medium scale. These data sets and research results are useful for policymakers in air pollution control administration to plan a more sustainable living environment.

SHB is seriously affected by the southeast monsoon and plum rain season in summer. Despite the high time resolution of the MODIS images (daily), these images are often influenced by massive cloud cover in AOD inversion and PM$_{2.5}$ estimation. leading to poor estimated results on some days. Therefore, the replacement or supplement of these data (seriously disturbed by clouds) will be helpful for improving the accuracy of AOD inversion and PM$_{2.5}$ estimation. While the inversion AOD accuracy is high by the method of EDTA, the basic DTA method has certain requirements for the vegetation coverage in the region. In high surface reflectance areas, this method is only moderately effective.

Combining more suitable inversion methods according to different surface types could increase the accuracy.

Future investigations would be helpful in the following aspects: changes in particulate matter at a micro scale would improve the accuracy of AOD-PM$_{2.5}$ estimation models; problems of data loss and signal-noise ratio (caused by cloud and rainfall interference) could be anticipated in the development of multi-source spatial-temporal data fusion; for instance, we are trying to solve the single-source data in the product resolution and spatial-temporal coverage and improve the accuracy and reliability of estimated PM$_{2.5}$ data; improved estimation PM$_{2.5}$ data could be used to evaluate the population exposure risk to PM$_{2.5}$, health economic losses, and early warning and prevention, in order to provide scientific reference for policymakers for improving urban atmospheric pollution and living environments.

5. Conclusions

This study developed a framework to improve the spatial resolution of AOD and PM$_{2.5}$ dataset and present the health risk assessment from PM$_{2.5}$ pollution: first, we retrieve the daily AOD using MODIS remote sensing images, AERONET AOD data, and the Enhanced Dark Target Algorithm (EDTA). Then we mapped the monthly and seasonal AOD results at a spatial resolution of 1 km × 1 km. Second, we inferred the optimal relationship between retrieved AOD and observed PM$_{2.5}$ in four seasons, and spatial-temporal seasonal models were developed to estimate PM$_{2.5}$ concentration. According to geographical features and seasonal characteristics in the study area, we obtain seasonal PM$_{2.5}$ at 1-km grid level by GIS platform. Third, we assessed health risk from PM$_{2.5}$ pollution using high-accuracy population density data and the relative exposure risk model. Last, the usage and deficiency of PM$_{2.5}$ dataset and risk assessment results were discussed. Therefore, reasonable assessments on health risk from PM$_{2.5}$ pollution are important for improving public health and living environment.

Abbreviations

GIS	Geographic Information Systems
RS	Remote sensing
SDGs	Sustainable Development Goals
PM$_{2.5}$	fine particulate matter (a diameter of less than 2.5 μm)
GOES	Geostationary Operational Environmental Satellite
METOP	European new generation weather operational satellites
PARASOL	Polarization and Anisotropy of Reflectances for Atmospheric Sciences coupled with Observations from a Lidar
MODIS	Moderate-resolution Imaging Spectror

Int. J. Environ. Res. Public Health **2022**, *19*, 6154

21 of 24

AVHRR	Advanced Very High Resolution Radiometer
SeaWiFS	Sea-viewing Wide Field of View Sensor
POLDER	Polarization and Directionality of the Earth's Reflectances
AOD	Aerosol Optical Depth
GEOS	Geosynchronous Earth Orbit Satellite
RAMS	Regional Atmospheric Modeling System
GLM	Generalized Linear Model
GAM	Generalized Additive Models
GWR	Geographically Weighted Regression
ML	Machine Learning
DTA	Dark Target Algorithm
EDTA	Enhanced Dark Target Algorithm
SHB	Shanghai-Hangzhou Bay
NSMS	National Standard Map Service platform in China
ESDC	Environmental Sciences and Data Center in China
NASA	National Aeronautics and Space Administration
LAADS	the Level-1 and Atmosphere Archive and Distribution System
AERONET	Aerosol Robotic Network
CEME	China Environmental Monitoring Center
LUT	Lookup Table
GCP	Ground Control Points
HDF	Hierarchical Data File

References

1. UN General Assembly. *Transforming our World: The 2030 Agenda for Sustainable Development*; United Nations: New York, NY, USA, 2015.
2. Zhang, N.; Zhang, A.Q.; Wang, L.; Nie, P. Fine particulate matter and body weight status among older adults in China: Impacts and pathways. *Health Place* **2021**, *69*, 102571. [CrossRef] [PubMed]
3. China Ministry of Ecological Environment. China's Ecological Environment Status Report 2016 (Extract). *Environ. Prot.* **2017**, *45*, 35–47.
4. China Ministry of Ecological Environment. *China's Ecological Environment Status Report 2017*; China Ministry of Ecological Environment: Beijing, China, 2018. Available online: https://english.mee.gov.cn/Resources/Reports/soe/SOEE2017/201808/P0 20180801597738742758.pdf (accessed on 31 March 2022).
5. China Ministry of Ecological Environment. *China's Ecological Environment Status Report 2018*; China Ministry of Ecological Environment: Beijing, China, 2018. Available online: https://english.mee.gov.cn/Resources/Reports/soe/2018SOEE/202012/P0 20201215585208685493.pdf (accessed on 31 March 2022).
6. China Ministry of Ecological Environment. *China's Ecological Environment Status Report 2019*; China Ministry of Ecological Environment: Beijing, China, 2019. Available online: https://english.mee.gov.cn/Resources/Reports/soe/SOEE2019/202012/P0 20201215587453898053.pdf (accessed on 31 March 2022).
7. China Ministry of Ecological Environment. *China's Ecological Environment Status Report 2020 (Extract)*; China Ministry of Ecological Environment: Beijing, China, 2021; pp. 47–68.
8. Son, J.Y.; Lane, K.J.; Miranda, M.L.; Bell, M.L. Health disparities attributable to air pollutant exposure in North Carolina: Influence of residential environmental and social factors. *Health Place* **2020**, *62*, 102287. [CrossRef] [PubMed]
9. Bates, J.T.; Weber, R.J.; Abrams, J.; Verma, V.; Fang, T.; Klein, M.; Stricklan, M.J.; Sarnat, S.E.; Chang, H.H.; Mulholland, J.A.; et al. Reactive oxygen species generation linked to sources of atmospheric particulate matter and cardiorespiratory effects. *Environ. Sci. Technol.* **2015**, *49*, 13605–13612. [CrossRef] [PubMed]
10. Buteau, S.; Goldberg, M.S. A structured review of panel studies used to investigate associations between ambient air pollution and heart rate variability. *Environ. Res.* **2016**, *148*, 207–247. [CrossRef]
11. Wang, C.C.; Tu, Y.F.; Yu, Z.L.; Lu, R.Z. PM2.5 and cardiovascular diseases in the elderly: An overview. *Int. J. Environ. Res. Public Health* **2015**, *12*, 8187–8197. [CrossRef]
12. Chi, R.; Li, H.Y.; Wang, Q.; Zhai, Q.R.; Wang, D.D.; Wu, M.; Liu, Q.C.; Wu, S.W.; Ma, Q.B.; Deng, F.R.; et al. Association of emergency room visits for respiratory diseases with sources of ambient PM2.5. *J. Environ. Sci.* **2019**, *86*, 154–163. [CrossRef]
13. Guan, W.J.; Zheng, X.Y.; Chung, K.F.; Zhong, N.S. Impact of air pollution on the burden of chronic respiratory diseases in China: Time for urgent action. *Lancet* **2016**, *388*, 1939–1951. [CrossRef]
14. Gorai, A.; Tuluri, F.; Tchounwou, P. A GIS based approach for assessing the association between air pollution and asthma in New York State, USA. *Int. J. Environ. Res. Public Health* **2014**, *11*, 4845–4869. [CrossRef]
15. Perera, F.P.; Tang, D.; Wang, S.; Vishnevetsky, J.; Zhang, B.Z.; Diaz, D.; Camann, D.; Rauh, V. Prenatal polycyclic aromatic hydrocarbon (PAH) exposure and child behavior at age 6–7 years. *Environ. Health Perspect.* **2012**, *120*, 921–926. [CrossRef]

Int. J. Environ. Res. Public Health **2022**, *19*, 6154

22 of 24

16. Zeng, Z.J.; Huo, X.; Wang, Q.H.; Wang, C.Y.; Hylkema, M.H.; Xu, X.J. PM2.5-bound PAHs exposure linked with low plasma insulin-like growth factor 1 levels and reduced child height. *Environ. Int.* **2020**, *138*, 105660. [CrossRef] [PubMed]

17. Kim, C.; Jung, S.H.; Kang, D.R.; Kim, H.C.; Moon, K.T.; Hur, N.W.; Shin, D.C.; Suh, L. Ambient particulate matter as a risk factor for suicide. *Am. J. Psychiatry* **2010**, *167*, 1100–1107. [CrossRef] [PubMed]

18. Sass, V.; Kravitz, W.N.; Karceski, S.M.; Hajat, A.; Crowder, K.; Takeuchi, D. The effects of air pollution on individual psychological distress. *Health Place* **2017**, *48*, 72–79. [CrossRef] [PubMed]

19. Vert, C.; Sánchez-Benavides, G.; Martínez, D.; Gotsens, X.; Gramunt, N.; Cirach, M.; Molinuevo, J.L.; Sunyer, J.; Nieuwenhuijsen, M.J.; Crous-Bou, M.; et al. Effect of long-term exposure to air pollution on anxiety and depression in adults: A cross-sectional study. *Int. J. Hyg. Environ. Health* **2017**, *220*, 1074–1080. [CrossRef]

20. Herbreteau, V.; Salem, G.; Souris, M.; Hugot, J.P.; Gonzalez, J.P. Thirty years of use and improvement of remote sensing, applied to epidemiology: From early promises to lasting frustration. *Health Place* **2007**, *13*, 400–403. [CrossRef]

21. Maantay, J. Asthma and air pollution in the Bronx: Methodological and data considerations in using GIS for environmental justice and health research. *Health Place* **2007**, *13*, 32–56. [CrossRef]

22. Golly, B.; Waked, A.; Weber, S.; Samake, A.; Jacob, V.; Conil, S.; Rangognio, J.; Chrétien, E.; Vagnot, M.P.; Robic, P.Y.; et al. Organic markers and OC source apportionment for seasonal variations of PM2.5 at 5 rural sites in France. *Atmos. Environ.* **2019**, *198*, 142–157. [CrossRef]

23. Wang, Z.B.; Liang, L.W.; Wang, X.J. Spatio-temporal evolution patterns and influencing factors of PM2.5 in Chinese urban agglomerations. *Acta Geogr. Sin.* **2019**, *12*, 2614–2630.

24. Shen, Y.; Yao, L. PM2.5, population exposure and economic effects in urban agglomerations of China using ground-based monitoring data. *Int. J. Environ. Res. Public Health* **2017**, *14*, 716. [CrossRef]

25. Deuzé, J.L.; Bréon, F.M.; Devaux, C.; Goloub, P.; Herman, H.; Lafrance, B.; Maignan, F.; Marchand, A.; Nadal, F.; Perry, G.; et al. Remote sensing of aerosols over land surfaces from POLDER-ADEOS-1 polarized measurements. *J. Geophys. Res. Atmos.* **2001**, *106*, 4913–4926. [CrossRef]

26. Kaufman, Y.J.; Tanré, D.; Remer, L.A.; Vermote, E.F.; Chu, A.; Holben, B.N. Operational remote sensing of tropospheric aerosol over land from EOS moderate resolution imaging spectroradiometer. *J. Geophys. Res. Atmos.* **1997**, *102*, 17051–17067. [CrossRef]

27. Lyons, W.A.; Husar, R.B. SMS/GOES visible images detect a synoptic-scale air pollution episode. *Mon. Weather Rev.* **1976**, *104*, 1623–1626. [CrossRef]

28. Li, C.C.; Mao, J.T.; Liu, Q.H.; Yuan, Z.B.; Wang, M.H.; Liu, X.Y. Remote sensing aerosol with MODIS and the application of MODIS aerosol products. *Sci. China Ser. D* **2005**, *35*, 177–186.

29. Wang, Z.T.; Chen, L.F.; Zhang, Y.; Han, D. Urban surface aerosol monitoring using DDV method from MODIS Data. *Remote Sens. Technol. Appl.* **2008**, *23*, 284–288.

30. Kaufman, Y.J.; Sendra, C. Algorithm for automatic atmospheric corrections to visible and near-IR satellite imagery. *Int. J. Remote Sens.* **1988**, *9*, 1357–1381. [CrossRef]

31. Levy, R.C.; Remer, L.A.; Mattoo, S.; Vermote, E.F.; Kaufman, Y.J. Second-generation operational algorithm: Retrieval of aerosol properties over land from inversion of Moderate Resolution Imaging Spectroradiometer spectral reflectance. *J. Geophys. Res. Atmos.* **2007**, *112*, D13211. [CrossRef]

32. Holben, B.N.; Vermote, E.; Kaufman, Y.J.; Tanré, D.; Kalb, V. Aerosol retrieval over land from AVHRR data-application for atmospheric correction. *IEEE Trans. Geosci. Remote Sens.* **1992**, *30*, 212–222. [CrossRef]

33. Tanré, D.; Devaux, C.; Herman, M.; Santer, R.; Gac, J.Y. Radiative properties of desert aerosols by optical ground-based measurements at solar wavelengths. *J. Geophys. Res. Atmos.* **1988**, *93*, 14223–14231. [CrossRef]

34. Hsu, N.C.; Tsay, S.C.; King, M.D.; Herman, J.R. Aerosol properties over bright-reflecting source regions. *IEEE Trans. Geosci. Remote Sens.* **2004**, *42*, 557–569. [CrossRef]

35. Hsu, N.C.; Tsay, S.C.; King, M.D.; Herman, J.R. Deep blue retrievals of Asian aerosol properties during ACE-Asia. *IEEE Trans. Geosci. Remote Sens.* **2006**, *44*, 3180–3195. [CrossRef]

36. Lyapustin, A.; Martonchik, J.; Wang, Y.J.; Laszlo, I.; Korkin, S. Multiangle implementation of atmospheric correction (MAIAC): 1. Radiative transfer basis and look-up tables. *J. Geophys. Res. Atmos.* **2011**, *116*, D03210. [CrossRef]

37. Lyapustin, A.; Wang, Y.; Laszlo, I.; Kahn, R.; Korkin, S.; Remer, L.; Levy, R.; Reid, J.S. Multiangle implementation of atmospheric correction (MAIAC): 2. Aerosol algorithm. *J. Geophys. Res. Atmos.* **2011**, *116*, D03211. [CrossRef]

38. Guo, J.; Xia, F.; Zhang, Y.; Liu, H.; Li, J.; Lou, M.; He, J.; Yan, Y.; Wang, F.; Min, M.; et al. Impact of diurnal variability and meteorological factors on the PM2.5-AOD relationship: Implications for PM2.5 remote sensing. *Environ. Pollut.* **2017**, *221*, 94–104. [CrossRef] [PubMed]

39. Kumar, N. What can affect AOD-PM2.5 association? *Environ. Health Perspect.* **2010**, *118*, 109–110. [CrossRef] [PubMed]

40. Li, J.; Carlson, B.E.; Lacis, A.A. How well do satellite AOD observations represent the spatial and temporal variability of PM2.5 concentration for the United States? *Atmos. Environ.* **2015**, *102*, 260–273.

41. Donkelaar, A.V.; Martin, R.; Brauer, M.; Kahn, R.; Levy, R.; Verduzco, C.; Villeneuve, P.J. Global estimates of ambient fine particulate matter concentrations from satellite-based aerosol optical depth: Development and application. *Environ. Health Perspect.* **2010**, *118*, 847–855. [CrossRef]

42. Donkelaar, A.V.; Martin, R.V.; Park, R.J. Estimating ground-level PM2.5 with aerosol optical depth determined from satellite remote sensing. *J. Geophys. Res. Atmos.* **2006**, *111*, D21201. [CrossRef]
43. Liu, Y.; Park, R.J.; Jacob, D.J.; Li, Q.B.; Kilaru, V.; Sarnat, J.A. Mapping annual mean ground-level PM2.5 concentrations using multiangle imaging spectroradiometer aerosol optical thickness over the contiguous United States. *J. Geophys. Res. Atmos.* **2004**, *109*, D22. [CrossRef]
44. Tao, J.H.; Zhang, M.G.; Chen, L.F.; Wang, Z.F.; Su, L.; Ge, C.; Xiao, H.; Zou, M.M. A method to estimate concentrations of surface-level particulate matter using satellite-based aerosol optical thickness. *Sci. China Ser. D* **2013**, *8*, 1422–1433. [CrossRef]
45. Chen, L.F.; Tao, J.H.; Wang, Z.F.; Li, S.S.; Zhang, Y.; Fan, M.; Li, X.Y.; Yu, C.; Zou, M.M.; Su, L.; et al. Review of satellite remote sensing of air quality. *J. Atmos. Environ. Opt.* **2015**, *10*, 117–125.
46. Wang, Z.F.; Chen, L.F.; Tao, J.H.; Zhang, Y.; Su, B. Satellite-based estimation of regional particulate matter (PM) in Beijing using vertical-and-RH correcting method. *Remote Sens. Environ.* **2010**, *114*, 50–63. [CrossRef]
47. Li, C.C.; Mao, J.T.; Lau, A.K.H.; Yuan, Z.B.; Wang, M.H.; Liu, X.Y. Application of MODIS satellite products to the air pollution research in Beijing. *Sci. China Ser. D* **2005**, *48*, 209–219.
48. Chu, D.A.; Tsai, T.C.; Chen, J.P.; Chang, S.C.; Jeng, Y.J.; Chiang, W.L.; Lin, N.H. Interpreting aerosol lidar profiles to better estimate surface PM2.5 for columnar AOD measurements. *Atmos. Environ.* **2013**, *79*, 172–187. [CrossRef]
49. Hutchison, K.D.; Faruqui, S.J.; Smith, S. Improving correlations between MODIS aerosol optical thickness and ground-based PM2.5 observations through 3D spatial analyses. *Atmos. Environ.* **2008**, *42*, 530–543. [CrossRef]
50. Liu, Y.; Sarnat, J.A.; Kilaru, V.K.; Jacob, D.J.; Koutrakis, P. Estimating ground-level PM2.5 in the eastern United States using satellite remote sensing. *Environ. Sci. Technol.* **2005**, *39*, 3269–3278. [CrossRef]
51. Liu, Y.; Paciorek, C.J.; Koutrakis, P. Estimating regional spatial and temporal variability of PM2.5 concentrations using satellite data, meteorology, and land use information. *Environ. Health Perspect.* **2009**, *117*, 886–892. [CrossRef]
52. Strawa, A.W.; Chatfield, R.B.; Legg, M.; Scarnato, B.; Esswein, R. Improving retrievals of regional fine particulate matter concentrations from Moderate Resolution Imaging Spectroradiometer (MODIS) and Ozone Monitoring Instrument (OMI) multisatellite observations. *J. Air Waste Manag. Assoc.* **2013**, *63*, 1434–1446. [CrossRef]
53. Hu, X.F.; Waller, L.A.; AI-Hamdan, M.Z.; Crosson, W.L.; Estes, M.G., Jr.; Estes, S.M.; Quattrochi, D.A.; Sarnat, J.A.; Liu, Y. Estimating ground-level PM2.5 concentrations in the southeastern U.S. using geographically weighted regression. *Environ. Res.* **2013**, *121*, 1–21. [CrossRef]
54. Zhang, L.L.; Pan, J.H.; Lai, J.B.; Wei, S.M.; Wang, Y.; Zhang, D.H. Estimation of PM2.5 mass concentrations in Beijing-Tianjin-Hebei region based on geographically weighted regression and spatial downscaling method. *Acta Sci. Circum.* **2019**, *39*, 832–842. [CrossRef]
55. Chen, H.; Li, Q.; Zhang, Y.H.; Zhou, C.Y.; Wang, Z.T. Estimations of PM2.5 concentrations based on the method of geographically weighted regression. *Acta Sci. Circum.* **2016**, *36*, 2142–2151.
56. Deng, Y.; Liu, J.P.; Liu, Y.; Xu, S.H. Spatial distribution estimation of PM2.5 concentration in Beijing by applying Bayesian geographic weighted regression model. *Sci. Surv. Mapp.* **2018**, *43*, 39–45.
57. Zhai, L.; Li, S.; Zou, B.; Sang, H.Y.; Fang, X.; Xu, S. An improved geographically weighted regression model for PM2.5 concentration estimation in large areas. *Atmos. Environ.* **2018**, *181*, 145–154. [CrossRef]
58. Wei, J.; Huang, W.; Li, Z.Q.; Xue, W.H.; Peng, Y.R.; Sun, L. Estimating 1-km-resolution PM2.5 concentrations across China using the space-time random forest approach. *Remote Sens. Environ.* **2019**, *231*, 111221. [CrossRef]
59. Xue, T.; Zheng, Y.; Tong, D.; Zheng, B.; Li, X.; Zhu, T. Spatiotemporal continuous estimates of PM2.5 concentrations in China, 2000-2016: A machine learning method with inputs from satellites, chemical transport model, and ground observations. *Environ Int.* **2019**, *123*, 345–357. [CrossRef]
60. Wang, Z.F.; Zeng, Q.L.; Chen, L.F.; Tao, J.H.; Fan, M.; Zhang, Z.Y. Research progress of methodology and applications of PM2.5 estimation using satellite remote sensing. *Environ. Monit. Forew.* **2019**, *11*, 33–38.
61. Zou, B.; Peng, F.; Jiao, L.M.; Weng, M. GIS aided spatial zoning of high-resolution population exposure to air pollution. *Geomat. Inform. Sci. Wuhan Univ.* **2013**, *38*, 334–338.
62. Tong, L.G.; Li, X.M.; Huang, Z.; Zhang, J.; Tian, S.Z. Study on risk of population exposure to PM2.5 in Baotou City. *J. Arid Land Resour. Environ.* **2017**, *31*, 50–54.
63. Lu, M.; Schmitz, O.; Vaartjes, I.; Karssenberg, D. Activity-based air pollution exposure assessment: Differences between homemakers and cycling commuters. *Health Place* **2019**, *60*, 102233. [CrossRef]
64. Park, Y.M. Assessing personal exposure to traffic-related air pollution using individual travel-activity diary data and an on-road source air dispersion model. *Health Place* **2020**, *63*, 102351. [CrossRef]
65. Li, C.C.; Mao, J.T.; Liu, Q.H.; Chen, J.Z.; Yuan, Z.B.; Liu, X.Y.; Zhu, A.H.; Liu, G.Q. Distribution and seasonal variation of aerosol optical depth using MODIS data, eastern China. *Chin. Sci. Bull.* **2003**, *48*, 2094–2100.
66. Wang, L.L.; Xin, J.Y.; Wang, Y.S.; Li, Z.Q.; Wang, P.C.; Liu, G.R. Evaluation on the applicability of MODIS aerosol products in China from CSHNET. *Chin. Sci. Bull.* **2007**, *52*, 477–486.

Int. J. Environ. Res. Public Health **2022**, *19*, 6154

24 of 24

67. Holben, B.N.; Eck, T.F.; Slutsker, I.; Tanré, D.; Buis, J.P.; Setzer, A.; Vermote, E.; Reagan, J.A.; Kaufman, Y.J.; Nakajima, T.; et al. AERONET: A federated instrument network and data archive for aerosol characterization. *Remote Sens. Environ.* **1998**, *66*, 1–16. [CrossRef]

68. Tatem, A.J. WorldPop, open data for spatial demography. *Sci. Data* **2017**, *4*, 170004. [CrossRef] [PubMed]

69. Kaufman, Y.J.; Wald, A.E.; Remer, L.A.; Gao, B.C.; Li, R.R.; Flynn, L. The MODIS 2.1μm channel-correlation with visible reflectance for use in remote sensing of aerosol. *IEEE Trans. Geosci. Remote Sens.* **1997**, *35*, 1286–1298. [CrossRef]

70. Zhao, Z.Q.; Li, A.N.; Bian, J.H.; Huang, C.Q. An improved DDV method to retrieve AOT for HJ CCD image in typical mountainous areas. *Spectrosc. Spect. Anal.* **2015**, *35*, 1479–1487.

71. Ångström, A. The parameter of atmospheric turbidity. *Tellus* **1964**, *16*, 64–75. [CrossRef]

72. Kousa, A.; Oglesby, L.; Koistinen, K.; Künzli, N.; Jantunen, M. Exposure chain of urban air PM2.5: Associations between ambient fixed site, residential outdoor, indoor, workplace and personal exposures in four European cities in the EXPOLIS-study. *Atmos. Environ.* **2002**, *36*, 3031–3039. [CrossRef]

73. Zhang, L.L.; Pan, J.H. Spatial-temporal pattern of population exposure risk to PM2.5 in China. *China Environ. Sci.* **2020**, *40*, 7427.

74. Zhang, X.Y.; Hu, H.B. Risk assessment of exposure to PM2.5 in Beijing using multi-source data. *Acta Sci. Nat. Univ. Peking* **2018**, *54*, 1103–1113.